FULL PAPER

Improved Heat Spreading Performance of Functionalized Graphene in Microelectronic Device Application

Yong Zhang, Haoxue Han, Nan Wang, Pengtu Zhang, Yifeng Fu, Murali Murugesan, Michael Edwards, Kjell Jeppson, Sebastian Volz, and Johan Liu**

It is demonstrated that a graphene-based film (GBF) functionalized with silane molecules strongly enhances thermal performance. The resistance temperature detector results show that the inclusion of silane molecules doubles the heat spreading ability. Furthermore, molecular dynamics simulations show that the thermal conductivity (κ) of the GBF increased by 15%–56% with respect to the number density of molecules compared to that with the nonfunctionalized graphene substrate. This increase in κ is attributed to the enhanced in-plane heat conduction of the GBF, resulting from the simultaneous increase of the thermal resistance between the GBF and the functionalized substrate limiting cross-plane phonon scattering. Enhancement of the thermal performance by inserting silane-functionalized molecules is important for the development of next-generation electronic devices and proposed application of GBFs for thermal management.

1. Introduction

Self-heating is a critical issue that needs to be addressed immediately to improve the long-term reliability and performances of micro and nanoelectronic devices.[1–3] The development and search for low-cost highly heat conductive materials is a necessity for the next generation of electronics.[4] The integration of novel materials with high thermal conductivity such as carbon nanotubes (CNTs)[5,6] into the chips for cooling has been attempted. Similar efforts are now being devoted to integrating graphene-based materials[7,8] into thermal management applications. Graphene has many outstanding properties such as high electronic mobility,[9] excellent mechanical properties,[10] and high transparency;[11] with the very high intrinsic thermal conductivity of graphene being the most advantageous for using it as a heat dissipation material in electronic and optoelectronic devices.[12,13] The in-plane thermal conductivity of exfoliated and suspended graphene has been reported as high as 2000–5000 W m^{-1} K^{-1} in the literature.[4,12,14] The values are comparable to CNTs,[4,15,16] but higher than those reported for graphite[17] and diamond.[18]

Although the thermal conductivity of suspended graphene is very high at room temperature, the in-plane thermal conductivity of graphene decreases significantly when it is in contact with a substrate.[19] For instance, the in-plane thermal conductivity of single layer graphene (SLG) supported on amorphous silicon dioxide (SiO_2) was found to be ≈ 600 W m^{-1} K^{-1} at room temperature owing to phonon coupling and scattering.[12,20] Nevertheless, it is still higher than the values of common thin-film materials, such as copper and silicon, used in electronic applications.[21–24]

Due to their extraordinarily high in-plane thermal conductivity, graphene and few-layer graphene (FLG) have been intensely studied for use as a heat spreader both in experiments and simulations.[7,13,25–29] For instance, Yan et al.[7] used mechanically exfoliated few layer graphene derived from highly oriented pyrolytic graphite (HOPG) on a silicon carbide (SiC) substrate used for the thermal management of high-power Gallium nitride (GaN) transistors. It was recently reported that using thermal chemical vapor deposition (CVD) grown graphene as a heat spreader on a SiO_2 substrate redistributed the heat from localized hotspots.[26] In both cases, there were only weak van der Waals interactions between graphene and the substrates. Despite the thermal coupling between the AlGaN/GaN high electron mobility transistor (HEMT) and the FLG heat spreader fabricated above the device allowing for sufficient heat transfer,[7] the substrate roughness and quality of graphene affected this considerably.[26] Recently, the fabrication

Y. Zhang, Prof. K. Jeppson, Prof. J. Liu
SMIT Center
School of Automation and Mechanical Engineering
and Key State Laboratory of New Displays
and System Applications
Shanghai University
20 Chengzhong Road, Shanghai 201800, China
E-mail: johan.liu@chalmers.se
Y. Zhang, N. Wang, P. Zhang, Dr. M. Murugesan,
Dr. M. Edwards, Prof. K. Jeppson, Prof. J. Liu
BioNano Systems Laboratory
Department of Microtechnology and Nanoscience
Chalmers University of Technology
Kemivägen 9, SE-412 96 Gothenburg, Sweden
H. Han, Prof. S. Volz
CNRS, UPR 288 Laboratoire
d'Énergétique Moléculaire et Macroscopique
Combustion (EM2C), Grande Voie des Vignes
92295 Châtenay-Malabry, France
E-mail: haoxue.han@ecp.fr
H. Han, Prof. S. Volz
École Centrale Paris
Grande Voie des Vignes
92295 Châtenay-Malabry, France
Dr. Y. Fu
SHT Smart High Tech AB
Aschebergsgatan 46, SE-41133 Gothenburg, Sweden

DOI: 10.1002/adfm.201500990

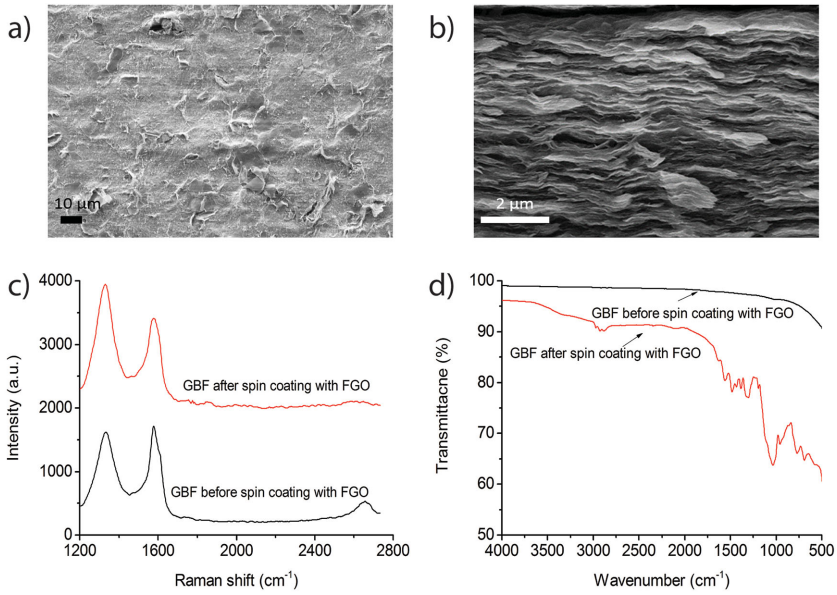

Figure 1. a) SEM image of the in-plane direction of the GBF. b) SEM image of the cross section of the GBF. c) Raman spectra of GBF before and after spin coating with FGO. d) FTIR spectra of GBF before and after spin coating with FGO.

of freestanding large area graphene-based films (GBFs),[30] graphene papers,[31] multilayer graphene/epoxy composite,[32] and graphene laminate,[33] all that can act as heat spreaders for electronics have been reported in the literature. However, compared to the monolayer or few layer graphene fabricated by mechanical exfoliation[7] or CVD[26] methods, these freestanding materials were poorly adhered to the substrate. Since only weak van der Waals interactions provide any adhesion, it results in poor thermal coupling between the freestanding materials and the substrates. Moreover, the existence of interfacial thermal contact resistances may have detrimental effects on the hotspot remediation even if the lateral thermal conductivity is very high.[34] Consequently, controlling the thermal boundary resistance and improving the contacts at the interface between graphene and the substrate are very important for both fundamental research and practical applications.[4,34]

In this article, the heat-spreading enhancement of a supported GBF with the addition of silane-functionalized molecules was studied. The molecules immobilized at the planar surface of graphene sheets form covalent bonds with silicon dioxide surfaces, which is useful for the heat transfer from the heat source. A resistance temperature detector (RTD) and infrared (IR) methods were both employed to evaluate the enhanced thermal performance. Molecular dynamics (MD) simulations were performed to support the experimental analysis. The details of the sample preparation are given in the Experimental Section.

2. Results and Discussion

Figure 1a,b contains typical scanning electron microscopy (SEM) images of the in-plane and out-of-plane of the GBF. By carefully controlling either the filtration volume or the concentration of graphene in the suspension by vacuum filtration, well aligned GBFs with different thickness were obtained. As is shown, the film in the in-plane direction was randomly stacked. However, the cross section shows a layer-by-layer structure in the vertical direction due to the flow-directed assembly of graphene layers with good orientations.[35] Moreover, vacuum filtration of the assembled GBF allowed the formation of highly aligned nanostructures, resulting in high lateral thermal properties (as shown in **Table 1**). The measurement of the in-plane thermal conductivity of GBFs with different thicknesses was carried out using the laser flash technique (Netzsch LFA 447). The thermal conductivity was determined from the equation of $\kappa = \alpha\rho C_p$, where α is the thermal diffusivity, ρ is the density of the sample, and C_p is the specific heat of the sample measured separately. The laser flash measurements showed that as the thickness of the films increases from 20 μm to 60 μm, the in-plane thermal conductivity reduces from 1642 W m^{-1} K^{-1} to 675 W m^{-1} K^{-1}. This decrease is due to an increase in the total defect number in the fabricated microstructure. These defects create obstacles for in-plane phonon propagation in the graphene sheets and hence reduce the high thermal conductivity.

Raman spectroscopy was performed on the GBF before and after spin coating the functionalized graphene oxide (FGO) layer (10–20 nm), where Figure 1c shows these respective Raman spectra. Before spin coating, the Raman spectra show the D band at 1334 cm^{-1}, G band at 1577 cm^{-1}, and the 2D band at 2657 cm^{-1}. The D band indicates the noise level, with the relatively intense D band signifying the presence of defects due to chemical reduction. However, after spin coating, the intensity ratio of I_D/I_G was 1.2, compared to that of 0.94 before spin coating, with this attributed to the presence of FGO on the GBF surface. Furthermore, the intensity ratio of I_{2D}/I_G is less than 1, indicating that the GBF has a multilayered structure.[36]

Fourier transform infrared spectroscopy (Spectrum Two, PerkinElmer) was also conducted to study the functional groups on the GBF before and after spin coating with FGO. As shown in Figure 1d, before spin coating FGO, there are no significant peaks between 2500–3000 cm^{-1} and 500–1500 cm^{-1}. However, after spin coating, the peaks around 2884 cm^{-1} and 2929 cm^{-1} were observed, which correspond to stretching vibrations

Table 1. In-plane thermal conductivity of GBFs with different thicknesses measured using the laser flash technique.

Thickness [μm]	Thermal diffusivity [mm^2 s^{-1}]	Specific heat [W kg^{-1} °C]	Density [g cm^{-3}]	In-plane thermal conductivity [W m^{-1} K^{-1}]
20	1800	0.76	1.20	1642
40	1100	0.71	1.58	1234
60	732	0.71	1.30	675

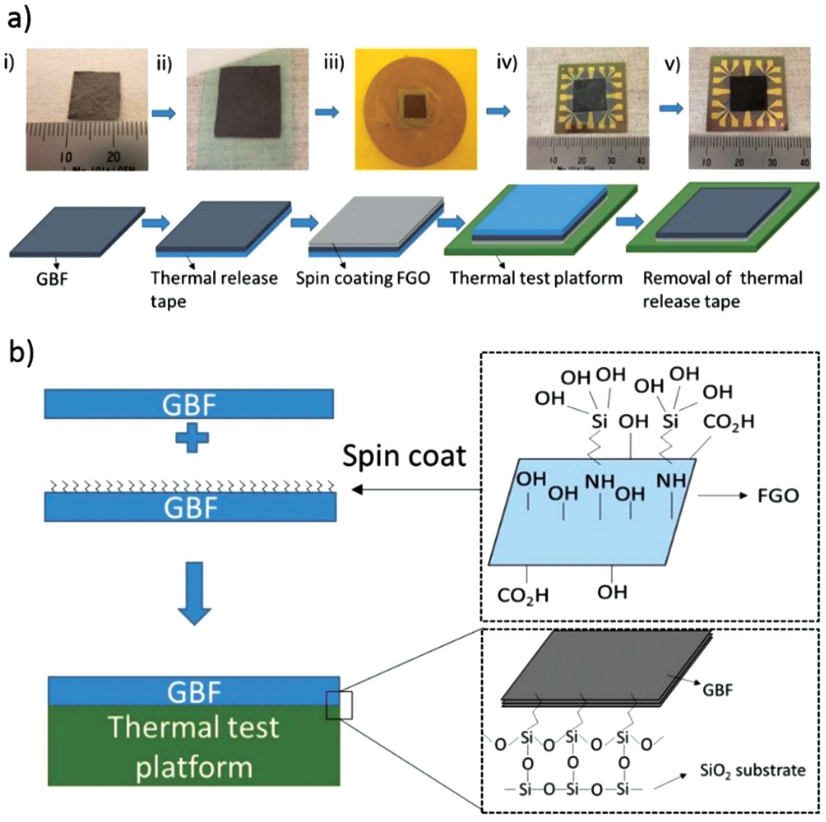

Figure 2. a) Schematic of the transfer process. (i) Start with a GBF. (ii) Transfer GBF onto thermal release tape. (iii) Spin coat FGO onto the GBF. (iv) Transfer GBF/FGO/thermal release tape-bundle onto the thermal test platform. (v) Removal of the thermal release tape. b) Mechanism of the surface bonding to a silicon dioxide substrate.

of —CH— and —CH_2— caused by (3-Aminopropyl) triethoxysilane (APTES) molecules. Moreover, peaks around 1034 cm^{-1} and 691 cm^{-1} indicate the presence of —Si—O—Si— and -Si-C-, which provides more evidence for functionalization.[37,38]

The thermal test platform (see the Experimental Section) was integrated with micro-Platinum (Pt)-based heating resistors and temperature sensors.[6,26,39] This setup acts as a test platform for simulating a real electronic component and to demonstrate the heat spreaders capability. A 20 µm GBF was chosen and cut into a small piece (1 cm × 1 cm), transferred onto thermal release tape, and then spin coated with a silane-FGO layer. After transfer of GBF/FGO/thermal release tape-bundle onto the thermal test platform, the thermal release tape was then removed by heating, and the whole process is described in **Figure 2**a. A copper (Cu) heat sink was mounted on the chip to remove the heat from the GBF. The Cu heat sink was mounted onto the test platform to conform to industry standards, where they are vital components in the cooling of electronic devices.[40] The heat sink provides extra cooling, which allows the test platform to be operated at the higher power densities now demanded by industry.[40–42]

The mechanism of the surface bonding onto a silicon dioxide substrate in this study is shown in Figure 2b. The silane-functionalized molecules located at the GBF/SiO_2 interface and the edge of graphene sheets, acting as a functional agent, react with the epoxy- and hydroxyl groups to form covalent bonds with the silicon dioxide surface. This results in the formation of molecular bridges between the GBF surface and the silicon dioxide layer.

Figure 3a,b shows the optical images of the thermal evaluation structure and the hotspot structure, respectively. A Pt microheater was heated by an electric current and its electric resistance was measured in situ, with the hotspot temperature obtained using Equation (1). The heat flux at the hotspot was adjusted by modifying the electric current. By using a graphene-based heat spreader, heat generated from the hotspot can be propagated onto a larger area, and then dissipated by a Cu sink, thus a temperature drop at the Pt hotspot was observed.

The thermal test platform was firstly calibrated; the obtained relationship between the resistance R (Ω) and the temperature T (°C), as shown in Figure 3c, is given as

$$R(T) = 0.21T + 112 \quad (1)$$

The thermal test platform showed good repeatability and provided an accuracy of ±0.5 °C, which is in agreement with previous literature.[26]

Figure 3d illustrates the thermal performance of the GBF heat spreader with and without silane-functionalized molecules. The temperature at the hotspot decreased from ≈146 °C to ≈140 °C ($\Delta t \approx 6$ °C) when a heat flux of 1500 W cm^{-2} was applied to the Pt hotspot, with a GBF providing dissipation. In contrast, by inserting the FGO between the GBF and substrate, the temperature at the hotspot was decreased from ≈146 °C to ≈134 °C ($\Delta t \approx 12$ °C). By using a FGO layer, the chip was cooled down by an additional 6 °C, which represents a doubling of performance.

This result indicates that with silane-functionalized molecules at the GBF/SiO_2 interface (as shown in Figure 2b), the heat generated at the hotspot is diminished when compared to the nonfunctionalized material at the graphene/SiO_2 interface. Due to the poor radiative capability of graphene,[43] heat generated by the Pt microheater flows mainly by conduction and convection. In this structure, where a chip mounted on a Cu heat sink, most of the heat flows from the graphene heat spreader to the Cu heat sink by conduction.

It was of interest to monitor the temperature profile on the surface of the thermal test platform. The surface temperature distribution, peak, and average temperature of the thermal test chip were examined using IR imaging camera (FLIR 655C). In order to achieve reliable measurement, graphite was sprayed onto the back side of the thermal test platform to ensure that the emissivity of the surface was constant. The IR intensity images of the temperature distribution on the thermal test chips surfaces were obtained at 120 mA. The images were taken after the chips reached a thermal steady state. The peak temperature

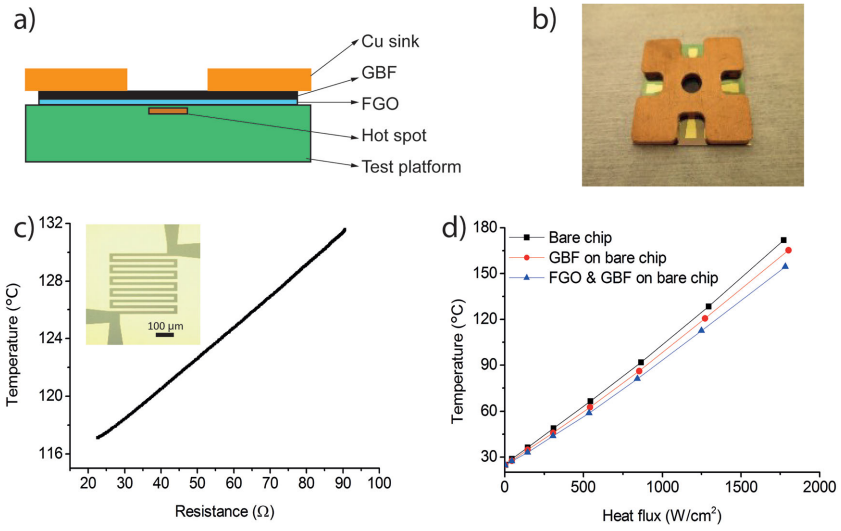

Figure 3. a) Basic schematic of thermal evaluation chip structure. b) Optical image of the thermal evaluation chip structure. c) Calibration results of the thermal evaluation chip. Inset: Optical microscopic image of the Pt microheater, acting as the hotspot at the center of a thermal test platform. d) Thermal performance of the samples.

of the chip surface for bare chip, GBF on bare chip, and FGO/GBF on bare chip was 121.9, 115.2, and 110.9 °C, respectively, with the respective average temperature distribution on the chip surface being 97.2, 93.8, and 91 °C, as shown in **Figure 4**. This result verifies that with silane-functionalized molecules at the GBF/SiO_2 interface, the heat generated in the circuit is lower compared to the no-silane case.

To rationalize the experimental results and evaluate the improvements in thermal performance of the GBF with the insertion of a silane-FGO layer, MD simulations were performed. The heat-spreading effects of a supported GBF film on top of silane-FGO were examined. A sketch of the chemical bonds of the silane molecule and the atomistic description of the FGO and the GBF above are shown in **Figure 5**a,b, respectively. In the MD simulations, the graphene oxide (GO) was replaced by pristine graphene to simplify the computation. This simplification is relevant since the oxidation of graphene has a minor impact on the cross-plane thermal transport of graphene sheets. Four graphene sheets are considered as the GBF. In the simulations, the graphene sheets are assumed to be defect-free and isotopically pure with dimensions of 10×10 nm at 300 K.

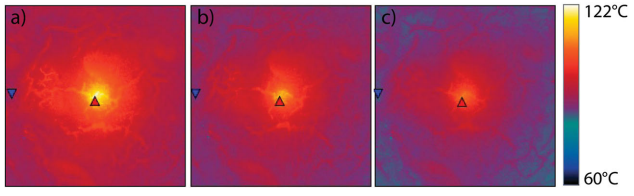

Figure 4. Infrared thermal imaging photographs of the chip surface. a) Temperature distribution on the surface of the bare chip. b) Temperature distribution on the surface of chip with a GBF. c) Temperature distribution on the surface of chip with both a GBF and FGO. The scale bar gives an estimation of the temperature associated with the different colors.

Figure 5c shows a plot of the in-plane thermal conductivity κ of the GBF and its associated thermal resistance R, with the silane functionalized graphene base layer as a function of the equivalent molecule number density in the silane functionalized GBF. Simulations show that the κ of the GBF increased by between 15% and 56% as a function of the number density of molecules compared with the non-silane functionalized substrate. The simultaneous increase of thermal resistance R between the GBF and the functionalized layer strongly inhibits cross-plane phonon scattering (see the Supporting Information) and thus enhances the in-plane heat conduction of the GBF resulting in an increase in κ. Previous works[44–46] show that the functionalization-introduced point defects destroy the intrinsically high in-plane thermal conductivity of graphene by strongly scattering phonons. In fact, we observed the same defect-induced decrease in the thermal conductivity of the graphene sheet adjacent to the functionalized substrate. However, the refrained substrate-graphene phonon scattering facilitates the overall in-plane phonon transport in the above graphene films. It is worth mentioning that the oscillations in the transmission spectrum may originate from phonon interferences within the alkane chain.[47,48]

Since both κ and R decrease with respect to the number density of the silane-based molecules and to explain the reduction in R, the molecules are considered as independent heat conductors connected in parallel to the graphene sheets in the small number density limit.[49] Thus, the thermal resistance decreases with the presence of more molecules that introduce more channels for heat flux. The κ of GBF decreases with respect to the molecule number density because the molecules act as heat conductors, resulting in lower thermal resistance and thus stronger cross-plane phonon scattering in the GBF.

It is noted that with a large number density of molecules, the thermal resistance falls lower than that without the presence of molecules in the functionalized graphene layers. However, the effective thermal conductivity of the GBF supported on the functionalized substrate remains enhanced by ≃15% compared to its value for the nonfunctionalization case. The molecule density effectively modifies the thermal conductivity of the supported graphene. Therefore, the functionalization of the GO support has a double advantage: it improves the thermal contact between the graphene and the support, while avoiding the detrimental effect introduced by the covalent bonds on the above graphene film. This directly validates the enhanced thermal spreading performance of the GBF based on the silane-FGO layer seen in the experiments.

3. Conclusion

A facile and scalable approach to fabricate large area free-standing GBFs with high thermal conductivity, as well as

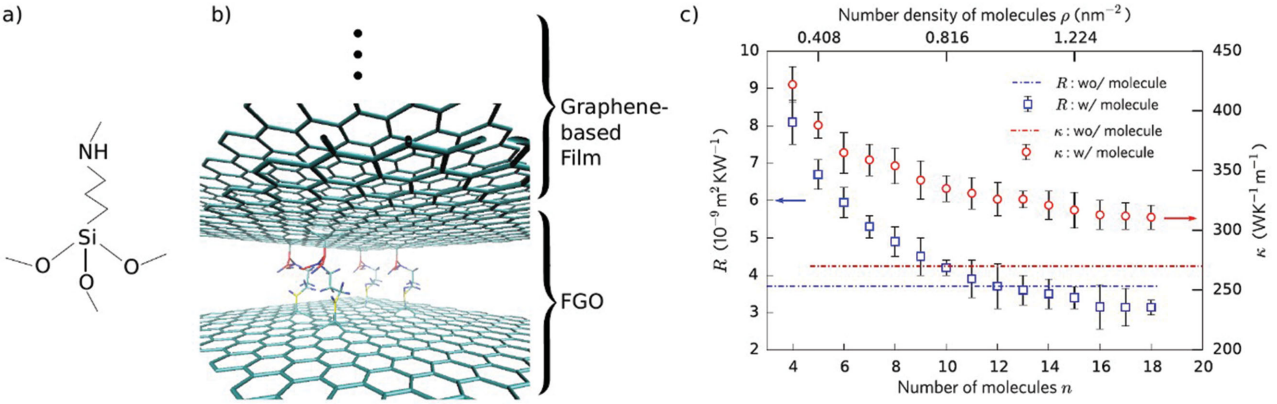

Figure 5. a) Sketch of the chemical bonds in the silane molecule. b) Atomistic description of the functionalized graphene and the GBF on the top (similar schematic as shown in Figure 1b). c) In-plane thermal conductivity (red circles) of the GBF and its associated thermal resistance R (blue rectangles) with the functionalized graphene substrate as a function of the number of molecules and the equivalent molecule number density in the functionalized graphene substrate. The red and blue dotted-dashed lines refer to the thermal conductivity and thermal resistance without silane functionalization on the substrate.

improved heat spreading performance of the GBF with the insertion of an FGO layer, is demonstrated. Experimental data indicates that the heat-spreading capability doubled by inserting the FGO layer. The reduced hotspot temperature suggests improved temperature uniformity across the chips, enhancing performance and lifetime for electronic devices. The simulation study also supports the experimental findings, which show that κ of the GBF increased by 15%–56% as a function of the number density of molecules compared with the nonfunctionalized graphene substrate. These findings broaden the understanding of the mechanism of heat transfer about a graphene-based heat spreader and may lead to advances in areas such as high-power light-emitting diodes (LEDs) and lasers. The proposed mechanisms are not just limited to GBFs made through the chemical reduction of GO but are also applicable to other types of GBFs, for example those made using liquid phase exfoliation or chemical vapor deposition methods. These findings facilitate a new understanding of functionalized graphene and will enable the integration of larger-area graphene into practical devices for thermal management.

4. Experimental Section

Preparation of Graphene-Based Film (GBF) and Functionalized Graphene Oxide (FGO): Typically, graphite (4 g, Sigma), H_2SO_4 (92 mL, 98% Conc.), $NaNO_3$ (2 g), and $KMnO_4$ (12 g) were used to prepare GO by adopting Hummer's method reported in the literature.[50] The obtained GO was further chemically reduced by excess L-ascorbic acid.[51] The GBF was prepared via vacuum filtration of a reduced GO solution with polycarbonate filter paper with a pore size of 3 μm. The film thickness was controlled by simply varying either the filtration volume or the concentration of the graphene sheets in the suspension. After the filter paper was dissolved in pure acetone, a freestanding GBF was obtained. The functionalization of GO was carried out by reacting GO powder, dicyclohexylcarbodiimide (DCC), and (3-Aminopropyl) triethoxysilane (APTES).[37,52] The epoxy groups located at the surface of the GO react with the amino group in APTES. At the same time, the silanol groups, which are generated by the hydrolysis of APTES, form covalent bonds with the hydroxyl groups at the basal plane of GO and on the surface of silicon dioxide.[53]

Building of the Thermal Test Platform: A Si (380 μm) wafer with a SiO_2 (400 nm) layer was used as a substrate. The SiO_2 layer represents the electrically insulating layer whereon the Pt-based heater and sensor were subsequently fabricated. The Si/SiO_2 substrate was cleaned using acetone, isopropyl alcohol, and distilled water. A standard lithography process was utilized to transfer the circuit pattern onto the substrate, and then titanium/platinum/gold (Ti/Pt/Au) films with respective layer thicknesses of 20/180/50 nm were evaporated using an e-beam evaporator (PVD 255, Kurt J. Lesker Company). This was followed by a lift off process to remove the residue. Finally, a 260 nm SiO_2 insulation layer was sputtered on the testing chip using a sputtering machine (MS150, FHR). Standard calibration was carried out using a resistance temperature detector (RTD) (LAB FACILITY PT100 XF-316-FAR) at various temperatures in a furnace. The four-point probe methodology was implemented to measure the electric resistance and the applied power of the Pt temperature sensor. The dimensions of the sensor was determined by its surface area of 400 μm × 420 μm, where the heat flux is equal to the applied power on hotspot divided by the hotspot area.

Measurement of Thermal Conductivity: The measurements of density at room temperature were measured using the Archimedes method. The density is defined as $\rho = 0.998 W_{air}/(W_{air} - W_{water})$. W_{air} is the mass of the sample in air and W_{water} is the mass of sample in water. The specific heat was measured by the Hot Disk transient method (TPS 2500) and thermal diffusivity was determined by the Nanoflash method (Netzsch LFA 447).

Supporting Information

Supporting Information is available from the Wiley Online Library or from the author.

Acknowledgements

This work was supported by Shanghai Science and Technology Program (12JC1403900) and NSFC (51272153), the SSF program "Scalable Nanomaterials and Solution Processable Thermoelectric Generators" with the contract No. EM11-0002, the SSF program "Carbon Based 3D GaN high speed electronic system" with the contract No. SE13-0061, and the EU FP7 program "Nanotherm". This work was also carried out within the Sustainable Production Initiative and Production Area of Advance at Chalmers.

Received: March 12, 2015
Revised: April 28, 2015
Published online: June 5, 2015

[1] O. Semenov, A. Vassighi, M. Sachdev, *IEEE Trans. Device Mater. Reliab.* **2006**, *6*, 17.
[2] R. Agaiby, A. G. O'Neill, S. H. Olsen, G. Eneman, P. Verheyen, R. Loo, C. Claeys, *IEEE Trans. Electron Devices* **2008**, *55*, 1568.
[3] S. E. Liu, J. S. Wang, Y. R. Lu, D. S. Huang, C. F. Huang, W. H. Hsieh, J. H. Lee, Y. S. Tsai, J. R. Shih, Y.-H. Lee, K. Wu, in *Reliability Physics Symp., 2014 IEEE Int.,* IEEE: New York, NY, **2014**, pp 4A.4.1–4A.4.4.
[4] A. A. Balandin, *Nat. Mater.* **2011**, *10*, 569.
[5] K. Kordás, G. Tóth, P. Moilanen, M. Kumpumäki, J. Vähäkangas, A. Uusimäki, R. Vajtai, P. M. Ajayan, *Appl. Phys. Lett.* **2007**, *90*, 123105.
[6] Y. Fu, N. Nabiollahi, T. Wang, S. Wang, Z. Hu, B. Carlberg, Y. Zhang, X. Wang, J. Liu, *Nanotechnology* **2012**, *23*, 045304.
[7] Z. Yan, G. Liu, J. M. Khan, A. A. Balandin, *Nat. Commun.* **2012**, *3*, 827.
[8] N. Han, T. Viet Cuong, M. Han, B. Deul Ryu, S. Chandramohan, J. Bae Park, J. Hye Kang, Y.-J. Park, K. Bok Ko, H. Yun Kim, H. Kyu Kim, J. Hyoung Ryu, Y. S. Katharria, C.-J. Choi, C.-H. Hong, *Nat. Commun.* **2013**, *4*, 1452.
[9] K. S. Novoselov, A. K. Geim, S. V. Morozov, D. Jiang, Y. Zhang, S. V. Dubonos, I. V. Grigorieva, A. A. Firsov, *Science* **2004**, *306*, 666.
[10] C. Lee, X. Wei, J. W. Kysar, J. Hone, *Science* **2008**, *321*, 385.
[11] R. R. Nair, P. Blake, A. N. Grigorenko, K. S. Novoselov, T. J. Booth, T. Stauber, N. M. R. Peres, A. K. Geim, *Science* **2008**, *320*, 1308.
[12] J. H. Seol, I. Jo, A. L. Moore, L. Lindsay, Z. H. Aitken, M. T. Pettes, X. Li, Z. Yao, R. Huang, D. Broido, N. Mingo, R. S. Ruoff, L. Shi, *Science* **2010**, *328*, 213.
[13] S. Subrina, D. Kotchetkov, A. A. Balandin, *IEEE Electron Device Lett.* **2009**, *30*, 1281.
[14] A. A. Balandin, S. Ghosh, W. Bao, I. Calizo, D. Teweldebrhan, F. Miao, C. N. Lau, *Nano Lett.* **2008**, *8*, 902.
[15] M. Fujii, X. Zhang, H. Xie, H. Ago, K. Takahashi, T. Ikuta, H. Abe, T. Shimizu, *Phys. Rev. Lett.* **2005**, *95*, 065502.
[16] C. Yu, L. Shi, Z. Yao, D. Li, A. Majumdar, *Nano Lett.* **2005**, *5*, 1842.
[17] G. Slack, *Phys. Rev.* **1962**, *127*, 694.
[18] G. A. Slack, *J. Appl. Phys.* **1964**, *35*, 3460.
[19] E. Pop, V. Varshney, A. K. Roy, *MRS Bull.* **2012**, *37*, 1273.
[20] B. Qiu, X. Ruan, *Appl. Phys. Lett.* **2012**, *100*, 193101.
[21] Y. S. Ju, K. E. Goodson, *Appl. Phys. Lett.* **1999**, *74*, 3005.
[22] Y. Yang, W. Liu, M. Asheghi, *Appl. Phys. Lett.* **2004**, *84*, 3121.
[23] W. Liu, Y. Yang, M. Asheghi, in *'06*The Tenth Intersociety Conference on Thermal and Thermomechanical Phenomena in Electronics Systems, 2006. ITHERM '06., IEEE, New York, NY **2006**, pp. 1171–1176.
[24] N. Stojanovic, J. Yun, E. B. K. Washington, J. M. Berg, M. W. Holtz, H. Temkin, *J. Microelectromech. Syst.* **2007**, *16*, 1269.
[25] S. Subrina, *J. Nanoelectron. Optoelectron.* **2010**, *5*, 281.
[26] Z. Gao, Y. Zhang, Y. Fu, M. M. F. Yuen, J. Liu, *Carbon* **2013**, *61*, 342.
[27] M.-H. Shih, L.-J. Li, Y.-C. Yang, H.-Y. Chou, C.-T. Lin, C.-Y. Su, *ACS Nano* **2013**, *7*, 10818.
[28] Y. Ni, Y. Chalopin, S. Volz, *Appl. Phys. Lett.* **2013**, *103*, 061906.
[29] S.-H. Bae, R. Shabani, J.-B. Lee, S.-J. Baeck, H. J. Cho, J.-H. Ahn, *IEEE Trans. Electron Devices* **2014**, *61*, 4171.
[30] P. Zhang, N. Wang, C. Zanden, L. Ye, Y. Fu, J. Liu, in *Electronic Components and Technology Conf. (ECTC), 2014 IEEE 64th* IEEE, Orlando, FL, **2014**, pp 459–463.
[31] G. Xin, H. Sun, T. Hu, H. R. Fard, X. Sun, N. Koratkar, T. Borca-Tasciuc, J. Lian, *Adv. Mater.* **2014**, *26*, 4521.
[32] Q. Li, Y. Guo, W. Li, S. Qiu, C. Zhu, X. Wei, M. Chen, C. Liu, S. Liao, Y. Gong, A. K. Mishra, L. Liu, *Chem. Mater.* **2014**, *26*, 4459.
[33] H. Malekpour, K.-H. Chang, J.-C. Chen, C.-Y. Lu, D. L. Nika, K. S. Novoselov, A. A. Balandin, *Nano Lett.* **2014**, *14*, 5155.
[34] C. Bachmann, A. Bar-Cohen, in *11th Intersociety Conf. on Thermal and Thermomechanical Phenomena in Electronic Systems, 2008. ITHERM 2008* IEEE, New York, NY **2008**, pp 238–247.
[35] A. R. Ranjbartoreh, B. Wang, X. Shen, G. Wang, *J. Appl. Phys.* **2011**, *109*, 014306.
[36] N.-W. Pu, C.-A. Wang, Y.-M. Liu, Y. Sung, D.-S. Wang, M.-D. Ger, *J. Taiwan Inst. Chem. Eng.* **2012**, *43*, 140.
[37] H. Yang, C. Shan, F. Li, D. Han, Q. Zhang, L. Niu, *Chem. Commun.* **2009**, *26*, 3880.
[38] Y. Lin, J. Jin, M. Song, *J. Mater. Chem.* **2011**, *21*, 3455.
[39] W. Qu, R. Green, M. Austin, *Meas. Sci. Technol.* **2000**, *11*, 1111.
[40] R. Mahajan, C. Chiu, G. Chrysler, *Proc. IEEE* **2006**, *94*, 1476.
[41] H. K. Ma, B. R. Chen, H. W. Lan, C. Y. Chao, in *26th Annual IEEE Semiconductor Thermal Measurement and Management Symp., 2010. SEMI-THERM 2010* IEEE, New York, NY **2010**, pp 289–298.
[42] H. Ren, Y. C. Zhou, L. F. Yang, T. Gao, *Appl. Mech. Mater.* **2013**, *475–476*, 1424.
[43] M. Freitag, H.-Y. Chiu, M. Steiner, V. Perebeinos, P. Avouris, *Nat. Nanotechnol.* **2010**, *5*, 497.
[44] S.-K. Chien, Y.-T. Yang, C.-K. Chen, *Appl. Phys. Lett.* **2011**, *98*, 033107.
[45] J. Y. Kim, J.-H. Lee, J. C. Grossman, *ACS Nano* **2012**, *6*, 9050.
[46] X. Mu, X. Wu, T. Zhang, D. B. Go, T. Luo, *Sci. Rep.* **2014**, *4*, 3909.
[47] H. Han, L. G. Potyomina, A. A. Darinskii, S. Volz, Y. A. Kosevich, *Phys. Rev. B* **2014**, *89*, 180301.
[48] H. Han, B. Li, S. Volz, Y. A. Kosevich, *Phys. Rev. Lett.* **2015**, *114*, 145501.
[49] T. Meier, F. Menges, P. Nirmalraj, H. Hölscher, H. Riel, B. Gotsmann, *Phys. Rev. Lett.* **2014**, *113*, 060801.
[50] W. S. Hummers, R. E. Offeman, *J. Am. Chem. Soc.* **1958**, *80*, 1339.
[51] J. Zhang, H. Yang, G. Shen, P. Cheng, J. Zhang, S. Guo, *Chem. Commun.* **2010**, *46*, 1112.
[52] R. M. Pasternack, S. Rivillon Amy, Y. J. Chabal, *Langmuir* **2008**, *24*, 12963.
[53] E. P. Plueddemann, *Silane Coupling Agents*, Springer, US **1991**, pp. 221–250.